

Automated, High-Resolution Micropipet Aspiration Reveals New Insight into the Physical Properties of Fluid Membranes

Volkmar Heinrich*[†] and Wiesława Rawicz[‡]

Boston University, Department of Biomedical Engineering,
44 Cummington Street, Boston, Massachusetts 02215, and University of British Columbia,
Department of Pathology, 2211 Wesbrook Mall, Vancouver, BC V6T2B5, Canada

Received September 2, 2004. In Final Form: December 8, 2004

We describe recent advances in our experimental approach to examine the physical properties of biological and artificial membranes by automated micropipet aspiration. New instrumentation allows us to apply fast yet precise tension protocols to membranes while continuously recording the membrane deformation with high-speed videomicroscopy. Robust algorithms for subpixel geometric measurements track the displacements of membrane edges with resolution of a few nanometers and enable us to determine changes of the membrane area and enclosed volume of pipet-aspirated cells or vesicles with exceptional accuracy. Experimentation and data analysis are greatly facilitated by custom-written software whose basic design is described here as well. Example measurements demonstrate how this technique has significantly improved the amount and reliability of data obtained by various types of micropipet-aspiration experiments, allowing us to study interesting aspects of membrane behavior that have eluded earlier techniques.

I. Introduction

Micron-sized pipets are not only a popular tool for cell handling, microinjection, or patch-clamp experiments, they also have proven exceptionally useful in direct measurements of the mechanical properties of membranes.^{1–4} Most of the currently known values of membrane elastic moduli for area dilation,^{2,5,6} shear,⁷ and bending^{6,8–11} as well as of membrane surface viscosity^{12–14} and interlayer friction¹⁴ have been established by various types of pipet-aspiration experiments. The recently introduced technique of dynamic tension spectroscopy (DTS)¹⁵ has opened a new dimension for measurements based on pipet aspiration, illuminating dynamic membrane behavior at extremely small energy levels where thermal activation strongly mediates tension-sensitive processes. Aimed to reveal the dynamic strength of membranes under varying ramps of tension, this technique has allowed us to characterize prominent details of the

energy landscape of pore formation in lipid membranes on the nanoscale and with millisecond time resolution. Furthermore, featuring a number of improvements over traditional, manual micropipet aspiration, our automated setup is well suited for any type of experiment that requires accurate monitoring of area or volume changes of pressurized membrane capsules. Example measurements that we can now carry out with considerably higher resolution and faster than previously include standard membrane-elasticity tests, measurements of membrane permeability, studies of the incorporation of amphiphilic molecules into membranes and of the tension dependence of lipid–protein interactions, or even the direct mechanical characterization of stress-activated membrane channels and tension-sensitive fluorophores. The instrument presented here should be useful not only for other research groups but also for emerging instructional facilities geared toward teaching experimental membrane mechanics to students of biophysics, physical chemistry, and bioengineering. The goal of this paper is to present the main ingredients (including software algorithms and data analysis) of the technique, providing enough detail to enable other researchers to adopt this setup, or parts of it, for their own needs. Several example measurements demonstrating the capabilities of this technique are included.

Generally, the instrument allows us to manipulate and study fluid membranes of spherical topology that enclose aqueous volumes, such as the envelopes of many biological cells as well as of artificial lipid vesicles. The extremely thin (few nanometers) lipid membranes are essentially two-dimensional surfaces that strongly disfavor free edges and exhibit specific elastic properties. The description of membrane deformations under stress is much easier when the surface is axisymmetric. A main advantage of pipet aspiration is that axial symmetry is imposed more or less by default, the pipet setting the axis of symmetry. Furthermore, because changes in area and volume of closed membranes are generally small during mechanical experiments, pressurization of membrane capsules by pipet aspiration often results in a trivial geometry where

* To whom correspondence should be addressed. E-mail: volkmar@bu.edu.

[†] Boston University.

[‡] University of British Columbia.

(1) Evans, E.; Skalak, R. *Mechanics and Thermodynamics of Biomembranes*; CRC Press: Boca Raton, FL, 1980.

(2) Evans, E.; Needham, D. *J. Phys. Chem.* **1987**, *91*, 4219–4228.

(3) Needham, D.; Zhelev, D. V. Use of micropipet manipulation techniques to measure the properties of giant vesicles. In *Giant Vesicles*; Walde, P., Luisi, P. L., Eds.; J. Wiley: New York, 1999.

(4) Henriksen, J. R.; Ipsen, J. H. *Eur. Phys. J. E* **2004**, *14*, 149–167.

(5) Kwok, R.; Evans, E. *Biophys. J.* **1981**, *35*, 637–652.

(6) Rawicz, W.; Olbrich, K. C.; McIntosh, T.; Needham, D.; Evans, E. *Biophys. J.* **2000**, *79*, 328–339.

(7) Waugh, R.; Evans, E. A. *Biophys. J.* **1979**, *26*, 115–131.

(8) Bo, L.; Waugh, R. E. *Biophys. J.* **1989**, *55*, 509–517.

(9) Evans, E.; Rawicz, W. *Phys. Rev. Lett.* **1990**, *64*, 2094–2097.

(10) Waugh, R. E.; Song, J.; Svetina, S.; Zeks, B. *Biophys. J.* **1992**, *61*, 974–982.

(11) Heinrich, V.; Waugh, R. E. *Ann. Biomed. Eng.* **1996**, *24*, 595–605.

(12) Hochmuth, R. M.; Wiles, H. C.; Evans, E. A.; McCown, J. T. *Biophys. J.* **1982**, *39*, 83–89.

(13) Waugh, R. E. *Biophys. J.* **1982**, *38*, 29–37.

(14) Evans, E.; Yeung, A. *Chem. Phys. Lipids* **1994**, *73*, 39–56.

(15) Evans, E.; Heinrich, V.; Ludwig, F.; Rawicz, W. *Biophys. J.* **2003**, *85*, 2342–2350.

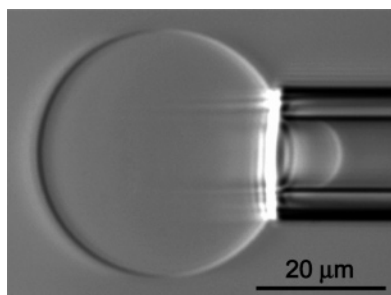


Figure 1. Videomicrograph of a partially pipet-aspirated phospholipid vesicle. The micropipet (entering from the right) is a hollow, cylindrical glass tube with an inner diameter of $\sim 10 \mu\text{m}$. The vesicle consists of a fluid membrane of spherical topology that encloses an aqueous sugar solution.

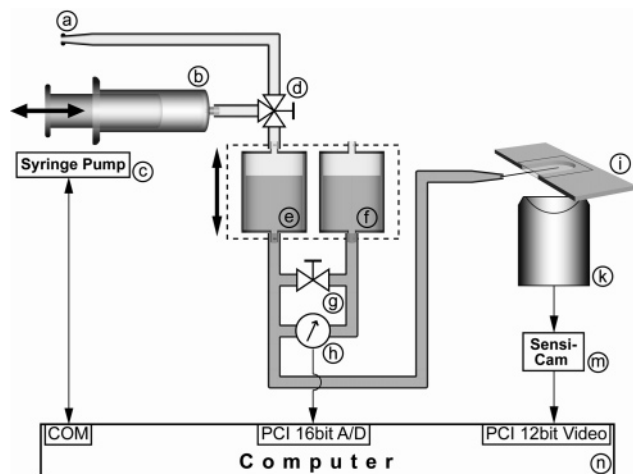


Figure 2. Schematic representation of the main parts of the instrument. The labeled components are listed in Table 1.

the membrane is composed exclusively of spherical and cylindrical parts. This is illustrated in Figure 1 showing a partially aspirated GUV, i.e., a giant *unilamellar* (as verified by membrane-elasticity measurements) vesicle whose membrane is a $\sim 3\text{--}4 \text{ nm}$ thick double layer of synthetic phospholipids.

II. Instrumentation

The instrument presented here has originally been designed for dynamic tension spectroscopy and automated membrane-elasticity studies. However, the principal setup will benefit any micropipet experiment in which a vesicle or cell is aspirated and its changing geometry analyzed. The change in geometry is typically caused by variations in the aspiration pressure or by a change in the environment of the aspirated membrane capsule, such as a step in buffer osmolarity. The main advantages of our instrument are the automated application of suction pressure, including linear pressure ramps as fast as $500 \text{ cm H}_2\text{O}$ per second ($\sim 5 \times 10^4$ pascals per second), and the analysis of geometry changes with submillisecond temporal and subpixel spatial resolution.

Figure 2 gives a schematic overview of the main components of our automated pipet-aspiration setup; its labeled parts are listed in Table 1. It combines three major subsystems that serve, respectively, to apply and measure pressure in a micropipet (parts a–i), to monitor micromanipulation and membrane deformation by videomicroscopy (parts k and m), and to remotely control and run experiments with custom-written software (part n). The following sections describe the parts of each subsystem in detail. Note that while we give the model numbers of

Table 1. List of the Main Components of the Instrument as Labeled in Figure 2

(a)	mouthpiece for hands-free pressure application
(b)	airtight syringe
(c)	motorized, computer controlled syringe pump
(d)	three-way valve
(e)	main water reservoir
(f)	reference water reservoir
(g)	two-way stop valve
(h)	differential pressure transducer
(i)	microscope chamber (polycarbonate) with U-shaped cutout to allow the pipet to enter (from left); coverslips are attached to top and bottom with vacuum grease
(k)	microscope objective
(m)	cooled 12 bit digital CCD camera; fast frame rate up to ~ 1500 fps
(n)	computer with interfaces to syringe pump, pressure transducer, and camera

our equipment for reference, it will often be possible to use alternative models or manufacturers to perform the same task.

1. Pressure Application and Measurement.

1.1. Micropipetting. Common to all measurements with this system is that a membrane capsule is picked up by suction pressure in a micropipet (thin black line, entering chamber i from the left in Figure 2). Suitable pipets are made from 1 mm (o.d.) borosilicate glass-tube capillaries (Kimble Glass, Inc., Vineland, NJ) that were pulled in a pipet puller (David Kopf Instruments, Tujunga, CA, model 730; or Sutter Instruments Co., Novato, CA, model P-87) to the desired tip diameter, typically in the range between 1 and $10 \mu\text{m}$ (i.d.). Our experiments require pipets with thin-walled, evenly broken tips that remain cylindrical for at least the length of the aspirated membrane portion (called in the following the “projection” of membrane into the pipet.) An evenly broken pipet tip can be achieved by different methods; our preferred technique uses a small amount of low-melting-point glass residing on a loop of the platinum heating wire of a microforge (Narishige International USA, Inc., East Meadow, NY, model MF-900 equipped with optional $35\times$ objective and $15\times$ eyepieces). This forge glass is heated until liquefied and the raw pipet tip is dipped into it by micromanipulation. The molten forge glass is allowed to flow upward inside the gradually widening capillary until it reaches the point where the pipet has the desired diameter. After covering also the outside of the pipet with molten forge glass almost up to this point, the heater is turned off, which causes the forge glass to solidify and retract and frequently results in an even break of the pipet.

The pipet is then backfilled with the required buffer using MicroFil syringe needles (World Precision Instruments, Inc., Sarasota, FL). A needle is inserted into the back opening of the pipet and pushed forward until it is wedged tightly into the converging pipet shaft, forming a seal. Buffer is infused forward until a small drop emerges from the pipet tip. The remaining pipet volume is filled by slowly backing up the needle while continuing to infuse buffer, carefully avoiding air bubbles.

Next, the back end of the filled pipet is inserted into a pipet-holding chuck (Research Instruments, Inc., Durham, NC) that allows the buffer in the pipet to merge with the water contained in the tubing of the pressure system. Thin, flexible tubing is needed for a tight seal around the port of the chuck (or back of the pipet) and for easy mounting of the chuck to a micromanipulator. It is important to find a good compromise for the length of this piece of tubing, because stepping up soon to wider, thicker-walled (but less flexible) tubing will provide a faster response to pressure changes.

Most measurements using the present setup are very sensitive to the pipet radius R_p . Depending on the desired accuracy (and on the experience of the operator), this radius is determined directly by inspection of a video-microscopic image or at the end of the experiment by a more reliable method. For example, insertion of a conical probe and measurement of its diameter at the pipet entrance generally gives more consistent results (requires a second micromanipulator). If the probe diameter changes very slowly and the relationship between the diameter of the probe and the distance from its tip has previously been established accurately (e.g., by electron microscopy), measuring the maximum insertion depth of the probe into pipets can result in much more precise values of pipet radii.

1.2. Pressure Measurement. The transducer (part h in Figure 2; Validyne Engineering, Northridge, CA, models DP15-20 and DP103-10) monitors the pressure difference between two partly filled water reservoirs (parts e and f). It accepts different diaphragms for optimum resolution and linearity in the desired pressure range. During its assembly, extreme care must be taken to avoid air bubbles. For example, we assemble all our transducers, along with the connected tubing, submerged in a tank of distilled and degassed water, and we later keep the system under slight positive pressure when not used. We mostly use Tygon tubing with 3/16 in. i.d. and 1/8 in. wall thickness to interconnect the parts of the pressure system.

Validyne offers a number of demodulators for their transducers; the single-channel model CD23 includes an LCD display as well as a $\pm 10V$ analogue output that can be interfaced with data-acquisition hardware in a computer. After assembly of a transducer (and occasionally afterward), each demodulator must be calibrated by applying a known pressure difference (see below) across the transducer's diaphragm and adjusting the zero and gain settings of the demodulator accordingly. Equilibration of the water level in the two reservoirs is possible at any time by opening the stop valve (part g). Of course, this valve must be closed during all actual pressure measurements.

1.3. Pressure Application. Pressure can be applied to the pipet in two principal ways: by lowering the vertical position of the water reservoir (part e) that is connected to the pipet or by closing off and evacuating the air volume above the water in this reservoir. In either case, the set pressure difference remains practically constant over long times because the volume of fluid flowing through the micron-size pipet is much too small to allow pressure equilibration, and flow ceases entirely as soon as a membrane capsule is aspirated and blocks the pipet.

Two vertical translators (Velmex, Inc., Bloomfield, NY) are used for changing reservoir heights. Figure 2 only indicates one of them (vertical double arrow); it moves both reservoirs simultaneously and is used to reset the pipet's zero pressure before each measurement. For this, both reservoirs should be open to the room air, which means that the three-way valve (part d) must not block the connection between the reservoir (part e) and the mouth piece (part a). Valve g is usually open as well. The pipet pressure is zeroed by adjusting the height of both reservoirs until flow in the pipet has stopped, as evidenced by the cessation of directed motion of small, free particles that have been picked up and are observed inside the pipet. Naturally, the pipet should be positioned at the same height (and preferably lateral position) as in the subsequent measurement.

A second vertical translator (preferably motorized; not shown in Figure 2) moves only the main reservoir (part

e) and sets the differential pressure between the two reservoirs. After proper zeroing, this is the same as the pressure difference between pipet and reference reservoir or between the pipet and the buffer surrounding it in the microscope chamber. This arrangement can also be used for direct pressure measurement (in units of water height) if the translator of the reservoir (part e) is equipped with a scale or encoder that reports the reservoir's vertical displacement. For small pressure ranges, this even allows calibration of the gain of the pressure transducer. For larger pressure ranges, deformation of the tubing connecting the reservoir (part e) with the pipet is hard to avoid during extended reservoir translation; transducer calibration in this case should be done using an independent manometer.

Manual evacuation of the air volume above the water in the main reservoir via a mouthpiece has long been used for hands-free micropipet manipulation of small objects. Crucial for DTS measurements, we have automated the creation of a vacuum by adding a bidirectional, computer-controllable syringe pump (part c in Figure 2; Harvard Apparatus, Inc., Holliston, MA, model PHD 2000 Infuse/Withdraw High Force) that can hold one or two large syringes (part b). The pump allows the user to set the infusing and withdrawing rates as well as the target volume either manually or by computer. Although the handmade glass syringes (Yale hypodermic syringe; Becton, Dickinson & Co., Franklin Lakes, NJ) are very hard to mount properly on the pump's syringe rack, we prefer them because of their smooth and easy plunger motion. Naturally, the port of valve d toward the mouthpiece (part a) must be closed whenever the syringe pump is used for pipet pressurization.

Fast pressure ramps require that the rate of change of the enclosed air volume be as large as possible. In addition to high pump speeds, our setup achieves this by using two large (50 mL) syringes and by reducing the total air volume through minimization of the air space above the reservoir's water and inside the tubing that connects pump and reservoir. The syringe pump is only capable of (piecewise) constant speeds during infusion and withdrawal, providing a more or less linear change in air volume. On the other hand, the analysis of DTS measurements relies on linear pressure ramps, but the pressure of an ideal gas is inversely proportional to its volume. However, this is of little concern because the change in air volume remains small relative to the total volume in all DTS experiments, limiting operation to the small-deformation regime where pressure changes quasi-linearly. Note that the elasticity of the Tygon tubing acts to extend the linear pressure regime even farther.

2. Video Microscopy. An Axiovert inverted microscope (Carl Zeiss Microimaging, Inc., Thornwood, NY) is used in one of two configurations depending on the visibility of the studied membrane capsules. For inspection of pipet-aspirated GUVs (cf. Figure 1), the microscope was equipped with Hoffman modulation contrast optics (Modulation Optics, Inc., Greenvale, NY). Objects with more contrast such as red blood cells are observed with conventional brightfield optics. Microscope objectives with 20 \times , 40 \times , or 63 \times magnification and $\sim 4\times$ camera adapters (original Zeiss adapter or custom-made adapter that accepts an eyepiece) give video images with a final magnification in the approximate range of 0.04–0.12 $\mu\text{m}/\text{pixel}$. An accurate video-distance calibration using a microscale (stage graticule; Electron Microscopy Sciences, Fort Washington, PA) has to be performed whenever the overall magnification changes.

The choice of the micromanipulator holding the pipet should take into account that slow pressure ramps require stable pipet positioning with minimum drift on the time scale of minutes. For accurate measurements of the projection length of membrane into the pipet, the pipet must be oriented more or less perpendicular to the optical axis of the microscope. Thus, it has to be mounted very close and nearly parallel to the microscope stage, possibly via a custom-made pipet-holding adapter that attaches to the manipulator. Alternatively, when using a microscope with infinity-corrected optics, one can raise the objective with a tubular spacer, in addition to elevating the measurement chamber, allowing easy pipet access at its side. Note, however, that a small downward tilt of the pipet is needed to be able to reach the chamber bottom with the pipet tip. Currently, our 3D micromanipulator is a three-axis stage (Newport Corp., Irvine, CA, x - y - z stage of 461 series) that is mounted rigidly to the microscope base (e.g., to the nonmoving part of the microscope stage) and has been equipped with motorized micrometers (Thermo Oriol at Spectra Physics, Stratford, CT). The micrometers are interfaced to analogue channels of a computer D/A output card via a custom-built controller; their motion is controlled with a conventional 3D game joystick and custom-written software. This low-cost compromise provides very low pipet drift but suffers somewhat from the jerky movement and considerable backlash of the motorized micrometers.

As indicated in Figure 2, our main video camera is PCO's SensiCam (The Cooke Corp., Auburn Hills, MI, model Long Exposure equipped with optional external cooling fan to minimize vibrations). This camera can easily be substituted if only standard video speed is required; however, it is the SensiCam's FFR (fast frame rate) mode that allows us to study a membrane's dynamic response to very fast pressure ramps with sufficient (i.e. submillisecond) time resolution. To achieve this high frame rate, the video region of interest has to be reduced substantially, so that an additional video system is needed for continuous full-frame visual inspection on a second monitor (not shown in Figure 2). For this, our setup uses a combination of a B/W analogue camera operating at the standard video speed of 30 fps (DAGE-MTI, Inc., Michigan City, IN, models CCD-300T-RC and CCD-72) and a frame grabber (Matrox Electronic Systems Ltd., Dorval, Quebec, model Meteor-II).

While high-speed cameras with even higher frame rates are available, the SensiCam's relatively fast transfer of the video buffer to computer memory actually allows *continuous*, real-time image analysis at ~ 1500 fps, if the region of interest is small and the analysis not too time-consuming. In high-speed mode, we commonly use a region of interest of 16 or 32 full-length (640 pixels) video lines centered about the axis of symmetry, i.e., the pipet axis. This region is vertically binned into a single line before being read out from the camera, ensuring fastest-possible transfer speeds as well as a much-improved signal-to-noise ratio in the resulting one-dimensional, axial intensity profile. In this mode, the camera's inactive lines outside the chosen region of interest are not being cleared and have to be blacked out to prevent their exposure. This is achieved by an adjustable slit mask mounted close to the camera's CCD chip as part of a custom-modified $4\times$ microscope-to-camera adapter. This adapter also provides for lateral translation of the camera, which is necessary because the active lines in FFR mode must always be the top lines of the camera chip. Adjusting the camera position rather than the microscope chamber or pipet allows us to center the aspirated membrane capsule in the full-frame video display of the second camera.

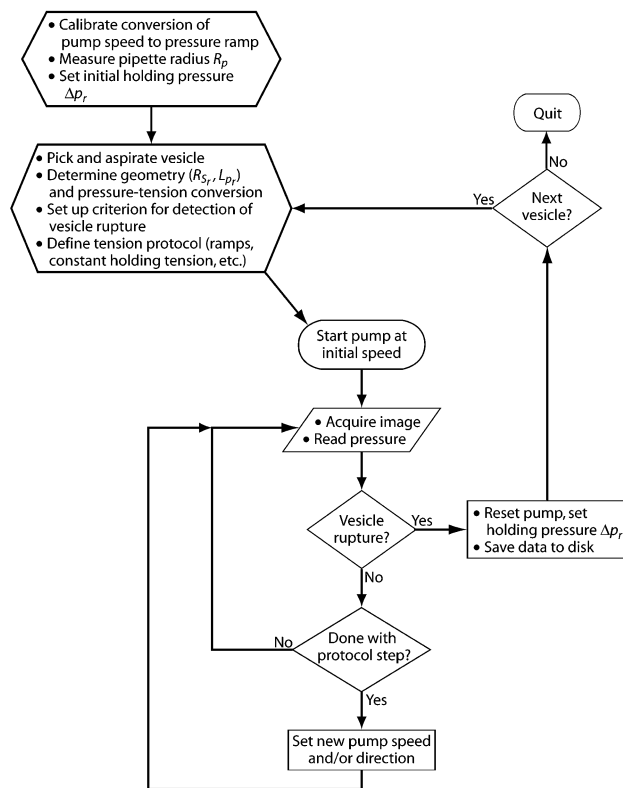


Figure 3. Flowchart of computer-assisted application of a predefined tension protocol to a pipet-aspirated vesicle. The experiment ends when the vesicle membrane ruptures, as is typical for DTS measurements.

3. Computer-Assisted Experimentation. After proper pressure calibration, a custom-written computer program (Visual C++ running on Microsoft Windows) controls the main aspects of each experiment. The program starts the pump at the desired initial speed, monitors the changing aspiration pressure for feedback-controlled execution of a predefined tension protocol, and records axial intensity profiles of the video image at a sampling rate of ~ 1.5 kHz. In our current setup, the intensity profiles are saved for later off-line analysis with very accurate but comparatively slow position-detection algorithms (see below). The program still monitors the video image during the actual experiment, but only to decide whether the aspirated membrane capsule is still intact. If the membrane ruptures, it quickly disappears into the pipet even at moderate aspiration pressures. In response, the program resets the pump to its original position, reducing the suction pressure to the initial value. The overall flow of program execution of an experiment ending with vesicle rupture is charted in Figure 3.

A fast personal computer (cf. Figure 2) communicates with the syringe pump (via the serial interface; requires a female-DB-9-to-male-RJ45 serial cable) and receives digitized input from the SensiCam and from the pressure transducer. The SensiCam includes its own digitizer/control board that is mounted in a PCI expansion slot of the computer. For automated pressure readings, the analogue voltage output of Validyne's demodulator is fed into an A/D converter, i.e., another PCI computer expansion card. Of three tested low-cost A/D cards (Quatech, Inc., Hudson, OH, model DAQ-12/PCI; Data Translation, Inc., Marlboro, MA, model DT 301; National Instruments Corp., Austin, TX, model NI PCI-6034E), only National Instruments' PCI-6034E lived up to our requirements (glitch-free operation, continuous readout at 10–100 kHz

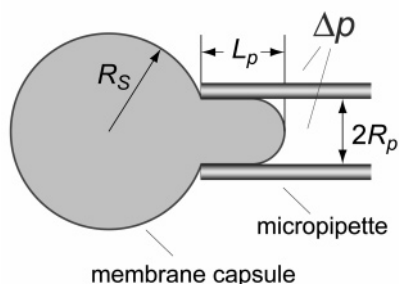


Figure 4. Sketch of a pipet-aspirated membrane capsule and illustration of the notation used in the text.

sampling rate, easy integration into our own program, and useful documentation). As the “raw” pressure unit, we use centimeter H₂O, allowing for easy and direct comparison of the transducer readout with the vertical distance between the water levels in the two reservoirs. Simultaneously, a second computer (not shown) runs two additional processes. One process reads the 3D joystick and controls the motorized micrometers for three-dimensional positioning of the pipet. The other uses Matrox’ MIL-Lite library to display the full-frame video provided by the second camera. A mouse-controlled tracker-rectangle overlay allows the user to perform simple distance measurements (horizontally and vertically) in the live image.

Prior to calibration of the conversion factor $C_{V_{\text{pump-to-}}V_{\text{press}}}$ (first step of measurement preparation in Figure 3), the transducer is “engaged” for pump pressurization, i.e., valve *d* is set to block the connection to the room air. This determines the total enclosed air volume and affects directly the relationship between pump speed and pressure ramp, so that $C_{V_{\text{pump-to-}}V_{\text{press}}}$ must be recalibrated whenever the pump’s initial position is changed. To establish this factor, the pump is driven at a moderate speed v_{pump} while the pressure is recorded as a function of time. The program fits a straight line to the upper two-thirds of the recorded pressure-vs-time data to obtain $v_{\text{press}} = d\Delta p/dt$ (Δp is pressure, and t is time), which gives $C_{V_{\text{pump-to-}}V_{\text{press}}} = v_{\text{press}}/v_{\text{pump}}$. After this point, the program has continuous pressure feedback, providing the operator, for example, with the ability to set a new pressure through software alone, by specifying both the new pressure value as well as the speed at which the pump will approach it.

After a suitable membrane capsule has been located in the microscope chamber, it is picked up in the pipet with low aspiration pressure and moved to the measurement position. The distance-measurement tool on the second video display is used to determine the reference values of the radius R_S , of the spherical membrane portion outside the pipet as well as the projection length L_p , of membrane into the pipet (cf. Figure 4) at the current holding pressure Δp . These values, along with the previously measured pipet radius R_p , establish the reference geometry of the vesicle or cell. They are also used by the main computer program to convert aspiration pressure into membrane tension (see eq 12 of the example section below). To perform a measurement at the desired *tension* rate, the software calculates the required pressure ramp for each given membrane capsule from this geometry and then translates it into pump speed via the conversion factor $C_{V_{\text{pump-to-}}V_{\text{press}}}$ established earlier. Other capabilities of the program include the option to design the time course of pressure application as a sequence of up and down ramps mixed with periods of constant holding pressure, etc. (“tension protocol”).

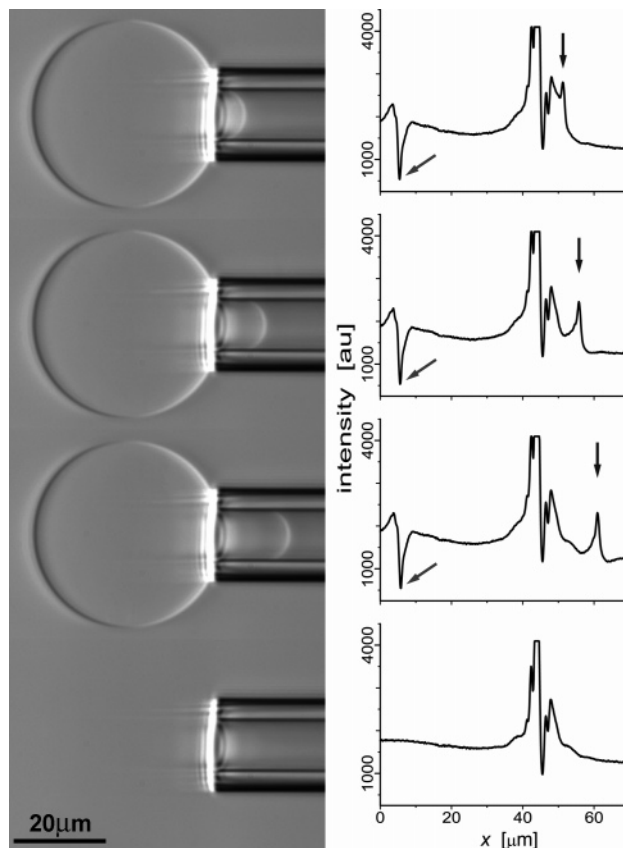


Figure 5. Series of video snapshots recorded during the aspiration of a phospholipid vesicle that was increasingly stressed by a linear pressure ramp (left). The last image was taken immediately after vesicle rupture at a high pressure, where buffer inflow into the pipet had quickly carried the membrane remnants out of the field of view. Recorded simultaneously were axial intensity curves (right) obtained for each frame by binning 32 video lines centered about the pipet axis into a single profile. A strong signal is produced by the diffraction pattern of the pipet tip. Clearly visible are also the membrane edges crossing the horizontal scanning region (marked by arrows).

Finally, the operator roughly specifies the image region on the main computer display that is occupied by the portion of the membrane capsule outside the pipet. As long as the maximum intensity difference between this region and the image background is greater than a user-selectable threshold, the program “assumes” that the membrane is still present and intact.

The membrane tension at the moment of rupture, measured for a given tension-loading rate, is the primary result of individual DTS tests. In parallel, axial intensity profiles (Figure 5; see also next section) are recorded for later analysis of the pressure dependence of the projection length L_p and the outer radius R_S . These values describe the deformation of the aspirated membrane capsule at a given tension and are needed in most studies of physical membrane properties.

III. Image Analysis

The recorded axial intensity profiles contain characteristic signatures of the diffraction patterns of the membrane edges (labeled by arrows in Figure 5) and of the pipet tip. Displacements of these signatures in subsequent intensity profiles reflect geometry changes of the membrane capsule, generally as a function of the aspiration pressure and of time. A separate data-analysis program establishes the membrane deformation with

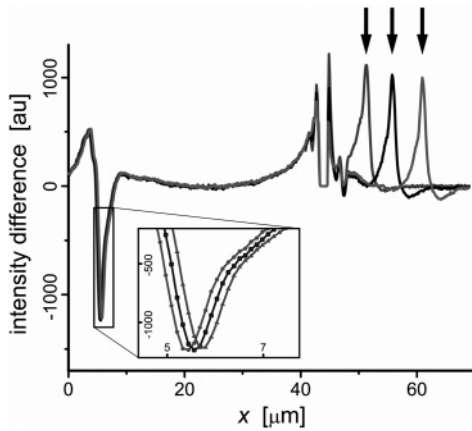


Figure 6. Superposition of the first three intensity profiles of Figure 5 after subtraction of the last, “background” profile. Arrows mark the movement of the membrane-projection edge in the pipet, whereas the considerably smaller displacements of the outer vesicle edge are enlarged in the inset.

subpixel accuracy and refines the moment of rupture with submillisecond resolution if necessary. The analysis program loads and displays the intensity profiles, allowing the user to flip through them sequentially or to jump to a particular profile. The last profile of each measurement was usually recorded after the membrane capsule had ruptured and disappeared, in which case it contains the intensity pattern of the pipet alone (see, for example, the bottom image and profile of Figure 5). As an option of the analysis program, this background profile may be subtracted from all other profiles, revealing enhanced signatures of the moving membrane edges as demonstrated in Figure 6.

Out of a multitude of potentially suitable, one-dimensional pattern-tracking algorithms, we have currently adopted approaches that are reasonably fast and accurate, as well as sufficiently robust to cope with a noisy and changing pattern moving on a possibly uneven background. First, the analysis program lets the user pick a number of search regions, each of which contains a particular feature to be tracked. This number is usually (but not restricted to) three, where the patterns correspond to the outer edge of the vesicle, the edge of the projection length in the pipet, and a prominent feature of the diffraction pattern of the pipet tip. The motion of the latter feature is used to monitor pipet drift in the axial (x) direction, so that the membrane-edge positions can be corrected for any such drift. (Note that pipet drift is best established using the *unaltered* intensity profiles, which makes it necessary to analyze the same profile sequence twice if the membrane edges are to be tracked *after* subtraction (as in Figure 6) of the last profile from the original intensity profiles.)

Next, the data range for each search region is selected interactively, and a smoothed, continuous representation $I(x)$ of the intensity data $\{x_j, I_j\}$ of each search region is calculated. Position detection based on the examination of $I(x)$ has two major advantages: the data smoothing reduces noise, and a continuous intensity representation overcomes the restriction to the discrete positions of pixel-based tracking algorithms. Moreover, working with $I(x)$ adds the ability to do most calculations in a straightforward, analytical manner.

In more detail, the program uses the FFTW library¹⁶ (see also <http://www.fftw.org>) to compute the discrete

Fourier transform $\mathcal{F}(I_j) = Z_k = A_k + B_k i$ ($0 \leq j, k \leq n - 1$) of the intensity data in a given search region. Here, n is the total number of data points in the region, and A_k, B_k are the real and imaginary part of the complex transform. Since the original intensity data I_j are real, the Fourier transform is Hermitian, i.e., $Z_k = Z_{n-k}^*$ for $k > 0$. The inverse transform $\mathcal{F}^{-1}(Z_k)$ provides a decomposition of the intensity data in a series of trigonometric functions, written in real numbers as

$$I_j = A_0 + 2 \sum_{k=1}^{\lfloor n/2 \rfloor} \left[A_k \cos\left(2\pi j \frac{k}{n}\right) - B_k \sin\left(2\pi j \frac{k}{n}\right) \right] \quad (1)$$

where $\lfloor c \rfloor$ denotes the greatest integer less than or equal to c . Note that for even n , a dummy coefficient $B_{n/2} = 0$ has been introduced in eq 1 for convenience. A smoothed version of the intensity data is obtained by applying a Gaussian filter to the Fourier coefficients, i.e.,

$$\tilde{A}_k = A_k \exp[-(k/w)^2] \quad \text{and} \quad \tilde{B}_k = B_k \exp[-(k/w)^2] \quad (2)$$

($1 \leq w \leq n$), and by replacing the original coefficients in eq 1 with those of eq 2. The transition from the resulting smoothed but still discrete intensity profile to a continuous representation is made through the substitution

$$j \rightarrow (n - 1) \frac{x - x_0}{x_{n-1} - x_0}$$

Abbreviating

$$\frac{1}{s} \equiv \frac{2\pi}{x_{n-1} - x_0} \frac{n - 1}{n}$$

we find for any real x within the search region given by $x_0 \leq x \leq x_{n-1}$

$$I(x) = \tilde{A}_0 + 2 \sum_{k=1}^{\lfloor n/2 \rfloor} \left[\tilde{A}_k \cos\left(\frac{x - x_0}{s} k\right) - \tilde{B}_k \sin\left(\frac{x - x_0}{s} k\right) \right] \quad (3)$$

Equation 3 is the desired analytical, continuous, and smoothed representation of the original intensity data in a given search region, obtained with only one adjustable parameter: the width w of the Gaussian filter (cf. eq 2). It is important to keep in mind two potential problems of this approach. First, increasing w will give functions $I(x)$ that describe the original data more closely; however, these better representations will also be more oscillatory, which means that $I(x)$ is more likely to have multiple extrema and inflection points. If such features are used for pattern tracking, it is crucial to choose sufficiently small values for w (typically in the range of 3–5) to prevent the detected edge position from jumping artificially between two or more of these features. Second, unless one does a certain amount of zero-padding on both sides of the original intensity data, aliasing may cause significant deviations of eq 3 from the original data at the boundaries of the search region (cf. Figure 7). The central range of the search region, however, is little affected by this. It is more practical, therefore, to make the search region sufficiently large and to ensure that the sought feature is located near its center.

Then, one suitable pattern-tracking algorithm identifies the position of each moving membrane edge with the position of a particular local intensity feature, whose type had initially been chosen from a list of three available

(16) Frigo, M.; Johnson, S. G. *Proceedings of the ICASSP conference* 1998, 3, 1381–1384.

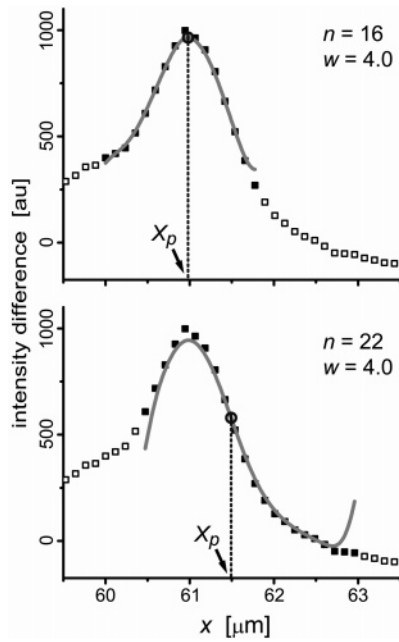


Figure 7. Illustration of automated tracking of the signature of a membrane edge in the recorded intensity profile. A characteristic part (consisting of n points) of the discrete intensity pattern of the membrane-projection edge (marked by arrows in Figure 6) is first replaced by a Fourier-smoothed (with Gaussian kernel of width w), continuous representation (solid line). Edge movement is then identified with the displacement of a chosen feature X_p of this curve, such as an intensity maximum (top) or an inflection point (bottom).

options: maximum, minimum, or inflection point of $I(x)$. Knowing all needed derivatives of $I(x)$ analytically, we use Newton’s method (Numerical Recipes,¹⁷ routine “rtsafe”) to find the root of the nonlinear equation $dI/dx = 0$ in the case of an extremum, or $d^2I/dx^2 = 0$ when searching for an inflection point (Figure 7). Once the desired position has been found, the data range is automatically readjusted for the next search, ensuring that the search region “slides” along the sequentially loaded profiles in accordance with the movement of the detected position.

A more advanced pattern-finding algorithm combines Fourier-smoothing of the intensity data with a “continuous cross-correlation” algorithm that locates a preselected and stored template within given search regions, providing even higher positional accuracy than the above procedure. In this approach, a characteristic central region (of width d_T) of the continuous and smoothed description (such as given by eq 3) of an initial data range is designated as the template $T(x)$. In all subsequent intensity profiles, the template’s position within equivalently represented search regions $S(x)$ (of width $d_S > d_T$) is determined by maximizing the normalized cross-correlation

$$C(x_T) = \frac{\langle ST \rangle - \langle S \rangle \langle T \rangle}{\sqrt{(\langle S^2 \rangle - \langle S \rangle^2)(\langle T^2 \rangle - \langle T \rangle^2)}} \quad (4)$$

with respect to the offset x_T ($0 \leq x_T \leq d_S - d_T$) between template and search region. Having expressed both the template $T(x)$ as well as the search region $S(x)$ in the same form as eq 3, the averages in eq 4 and their first and

(17) Press, W. H.; Teukolsky, S. A.; Vetterling, W. T.; Flannery, B. P. *Numerical Recipes in C++: The Art of Scientific Computing*; Cambridge University Press: Cambridge, U.K., 2002.

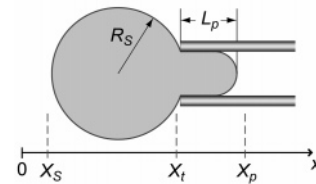


Figure 8. The same sketch as in Figure 4 is used to illustrate the three tracked positions X_S , X_p , and X_t . Note that these are the positions of intensity features that accurately trace any movement of the membrane edges and the pipet tip, respectively, but do not, in general, give the true, absolute positions of these edges.

second derivatives, needed to maximize $C(x_T)$, are easily calculated analytically from

$$\begin{aligned} \langle T \rangle &= \frac{1}{d_T} \int_0^{d_T} T(x) dx & \langle S \rangle &= \frac{1}{d_T} \int_{x_T}^{x_T+d_T} S(x) dx \\ \langle ST \rangle &= \frac{1}{d_T} \int_{x_T}^{x_T+d_T} S(x)T(x - x_T) dx \end{aligned}$$

etc. The only remaining numerical task to find x_T is to solve the nonlinear equation obtained from setting the first derivative of $C(x_T)$ to zero. All results presented below were obtained with this “continuous cross-correlation” approach.

Using the simultaneously recorded time and/or pressure data, we have thus determined the positions of the selected features in the intensity profiles as a function of time and of the aspiration pressure. In the following, we will concentrate on the positions X_S and X_p of the characteristic patterns of the outer edge of the spherical membrane capsule and of the edge of the projection of membrane in the pipet, respectively (Figure 8). Both of these positions may have been obtained by averaging more than one series of tracking data, and they have usually been corrected for axial pipet drift given by the trace of the pipet-tip position X_t (Figure 8). It is important to keep in mind that X_S and X_p are generally not the actual positions of the respective membrane edges but the somewhat arbitrarily chosen positions of particular features in the intensity signatures of these edges. Unfortunately, it seems largely unclear how to extract the true, absolute position of a ~ 4 nm thick membrane from the usually $> 1 \mu\text{m}$ wide (at our magnification, cf. Figures 5 and 6) optical signature generated by Hoffman modulation contrast microscopy. However, the tracked *displacements* of the intensity patterns reflect the actual edge *movement* very accurately. To obtain absolute edge positions, we rely on the operator’s initial measurement of the outer radius R_S , and of the projection length L_p , at a given reference pressure Δp_r (see above). Furthermore, we will continue to assume that the geometry of an aspirated membrane capsule is described with sufficient accuracy by spherical and cylindrical parts. The change in X_S equals the negative change in distance between the true membrane edge and the pipet entrance,

$$\Delta X_S = -\Delta(R_S + \sqrt{R_S^2 - R_p^2})$$

or

$$X_S = C_S - (R_S + \sqrt{R_S^2 - R_p^2}) \quad (5)$$

where $C_S \equiv X_{S_r} + R_{S_r} + \sqrt{R_{S_r}^2 - R_p^2}$ is a constant offset calculated using the initially measured reference values. Solving for the instantaneous radius R_S , we find the

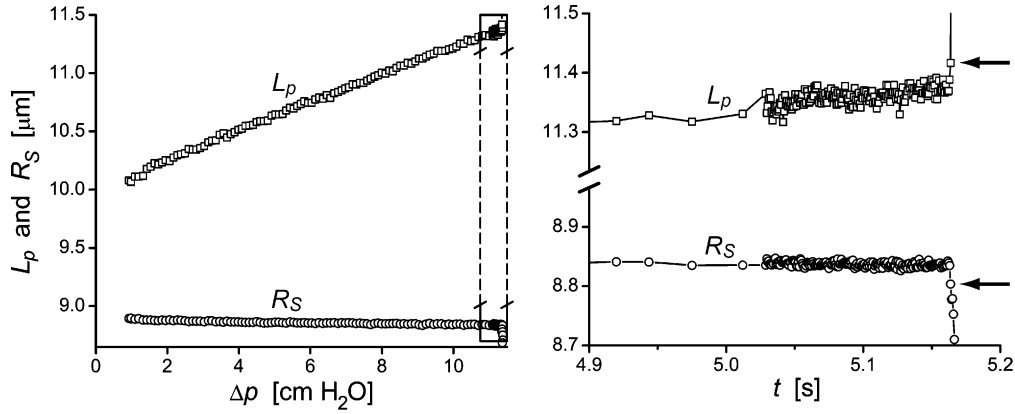


Figure 9. Traces of the outer radius R_S and the projection length L_p measured during automated pressurization of a vesicle whose membrane (made from the phospholipid di- C_{13} -PC) exhibited little cohesive strength and ruptured at a very low pressure. The inset (right) gives a more detailed view of the moment of rupture, plotting R_S and L_p as functions of time. To save disk space, only the last 300 data points were recorded at the full camera speed of ~ 1500 fps. Arrows identify the moment immediately after rupture.

following relationship between the position of the tracked feature and the radius:

$$R_S = \frac{1}{2} \left(C_S - X_S + \frac{R_p^2}{C_S - X_S} \right) \quad (6)$$

The analogous relationship for the projection length is simply

$$L_p = L_{p_r} + X_p - X_{p_r} \quad (7)$$

Having determined the outer radius and the projection length, the surface area and volume of a pipet-aspirated membrane capsule are

$$A(R_S, L_p) = 4\pi R_S^2 + 2\pi R_p L_p - \pi R_p^2 \quad (8)$$

$$V(R_S, L_p) = \frac{4}{3}\pi R_S^3 + \pi R_p^2 L_p - \frac{1}{3}\pi R_p^3 \quad (9)$$

(Equation 9 ignores that the volume of a small spherical cap at the pipet entrance is counted twice. The surface area of this cap, however, is not part of the total membrane area; it was approximated by a disk with radius R_p and subtracted in eq 8.)

IV. Example Measurements

A surprising amount of knowledge about the properties of membranes has been gathered from the inspection of geometry changes of pipet-aspirated membrane capsules under various conditions. Proper interpretation of the results of specialized experiments is often subtle and beyond this paper's emphasis on instrumentation. However, to demonstrate the capabilities of the current approach, this section presents a few example measurements that illustrate characteristic membrane behavior in response to an applied pressure ramp or a step in buffer osmolarity.

The first example (Figure 9) shows how the moment of lysis of a pressurized vesicle with a particularly weak-cohesive membrane is determined with submillisecond resolution in DTS measurements.¹⁵ When loaded by a pressure ramp, these vesicles often lyse at very low pressures where the monitored membrane edges remain visible for several video frames after rupture. In such cases, our simple test for the presence/absence of an intact membrane capsule (see above) may fail to identify the exact frame of rupture. Figure 9 demonstrates how the

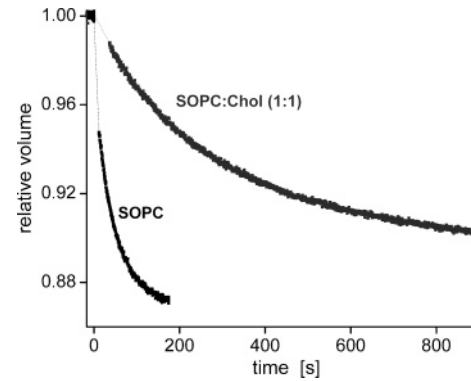


Figure 10. Changes of the fractional volume of two vesicles (made from the phospholipid 1-stearoyl-2-oleoyl-*sn*-glycero-3-phosphocholine (SOPC) and from a 1:1 mixture of SOPC and cholesterol) after identical steps in osmolarity of the surrounding sugar solution. Both vesicles were pipet-aspirated at a low (~ 2 cm H₂O) holding pressure. The break in the data curves marks the time needed to readjust our instrument after transferring the vesicles between the two different buffers. Reflecting water outflow, the observed volume changes demonstrate a ~ 10 -fold decrease in membrane permeability to water due to the presence of cholesterol.

needed information can still be extracted from the recorded intensity profiles. Here, we have used an optional feature of our software and saved only the last 300 (a user-selectable number) profiles at the maximum frame rate, whereas earlier profiles were stored at a lower data density to avoid unnecessarily large file sizes. The first frame after rupture is easily identified in the traces of both L_p and R_S , giving the moment of rupture to within less than 0.7 milliseconds.

Another example (Figure 10) shows the results of typical membrane-permeability tests for two different lipid membranes. These tests utilize the substantial rate difference between water and sugar transport across a membrane, which renders the membrane virtually impermeable to sugar on experimental time scales. Thus, following transfer from an isotonic into a hypertonic sugar solution, water outflow decreases the volume of a vesicle until a new osmotic balance is established. The physics of this process is described by a differential transport equation that, in general, cannot be solved analytically. Rather than having to match the numerical solution of this differential equation to the measured data, the smooth and dense data curves obtained with the present instrument enable us to *measure* the instantaneous derivative dV/dt at any time t directly and sufficiently accurate, which

simplifies the analysis of such measurements enormously. First results obtained with this approach, such as illustrated in Figure 10, are in excellent agreement with previously published values.^{18,19}

The final example illustrates the mechanical measurement that has become the standard method to establish the area-expansivity modulus K (units of force/length) of lipid membranes.^{2,5,6} It is based on the constitutive equation for isotropic area changes of a two-dimensional, fluid film,

$$\underline{\sigma} = K\alpha \quad (10)$$

which relates the two-dimensional area-dilational strain

$$\alpha \equiv \frac{dA - dA_0}{dA_0} = \frac{A - A_0}{A_0} \quad (11)$$

to the isotropic membrane tension $\underline{\sigma}$ (units of force/length). The subscript “0” refers to an unstressed membrane at an aspiration pressure of $\Delta p_0 = 0$. At equilibrium, the strain of a fluid, isotropic membrane is the same everywhere, which allows us to make the transition from local to global area stretch (second equality of eq 11). Normal force balance gives the membrane tension as

$$\underline{\sigma} = \frac{R_p}{1 - R_p/R_S} \frac{\Delta p}{2} \quad (12)$$

This important equation shows that the isotropic membrane tension $\underline{\sigma}$ is proportional to the aspiration pressure Δp and exhibits a relatively weak dependence on R_S . For our instrument this means that a quasi-linear pressure ramp, generated by the syringe pump, will translate into a quasi-linear ramp in membrane tension. Inversely, the pump speed required to achieve a desired DTS tension ramp can roughly be calculated from eq 12 (replacing R_S with the initially measured reference value R_{S_0}). The actual slope of tension versus time at the moment of rupture is later obtained as part of the DTS data analysis for each measurement.

To measure the dependence of the tension $\underline{\sigma}$ on the relative area expansion α , it has been customary up to now to monitor only changes in the projection length L_p of a pipet-aspirated membrane capsule as a function of the pressure Δp . Changes of the outer radius R_S were *calculated* from the assumption that the vesicle or cell volume remained constant during the experiment. This common assumption is not only an approximation that simplifies the data analysis significantly, it also appears fairly justified because the amount of water pushed mechanically out of a pressurized membrane capsule has to be very small if the buffer contains osmotically active solutes that cannot permeate the membrane, simply because otherwise the resulting osmotic imbalance would create a large counter pressure. However, the main obstacle to the direct experimental determination of the pressure dependence of R_S has been that changes in the outer radius are usually too small to be resolved with sufficient accuracy. In contrast, the high-resolution pattern-tracking algorithms introduced above have enabled us to determine R_S directly. For simplicity, however, we will first follow the traditional, constant-volume approach

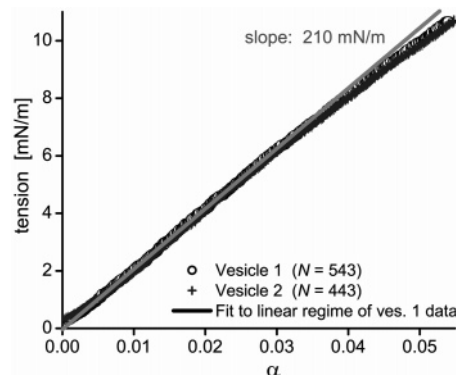


Figure 11. Isotropic membrane tension as a function of the relative area expansion for two vesicles (made from SOPC) subjected to a ramp in tension of ~ 0.4 mN/m/s. Assuming that the vesicle volume remained constant during pressurization, both quantities were obtained primarily from a total of N individual L_p -measurements. Near-linear constitutive behavior is observed over a large range of strain, where the proportionality constant provides a rough estimate of the area-expansivity modulus K . The apparent softening of the membranes at high tensions is addressed in the text.

and then use our R_S -measurements to examine the validity of this approximation.

Figure 11 shows plots of the tension as a function of the relative area expansion α for two different vesicles made from the same lipid, revealing, at moderate tensions, the expected linear dependence whose slope is a rough estimate of the area-expansivity modulus K . Its value agrees well with the results published for this often-used lipid. At high tensions, however, the slopes of both data plots deviate noticeably from the initial linear $\underline{\sigma}(\alpha)$ -dependence, seemingly reflecting a slight membrane softening at large stresses. While part of this observation may indeed be due to nonlinearities in the stress–strain relationship (eq 10), we should also inspect the effect of using the constant-volume assumption to calculate the instantaneous radius R_S that enters the calculation of both α as well as $\underline{\sigma}$. Figure 12A compares these calculated R_S -values with the measured radii that were extracted directly from the recorded intensity profiles. Even though for either vesicle, the two curves never deviate by more than ~ 60 nm (i.e., ~ 1 pixel in the video image), the observed difference is significant and shows that the volume does not actually remain constant during aspiration. The change of the measured volume is illustrated for both vesicles in Figure 12B. Note that this volume decrease will act to accelerate the growth of the projection length in the pipet. Naturally, if the membrane area is determined from the measured L_p -data alone (assuming a constant volume), this will be interpreted as an accelerated membrane expansion, which will indeed *appear* as an artificial softening of the membrane in plots such as shown in Figure 11. Of course, the same effect also reduces the slope in the quasi-linear regime of Figure 11, which means that the obtained K -value is a somewhat low estimate.

V. Conclusions

The present instrument has not only enabled us to perform traditional membrane experiments with much greater precision than before, it has also revealed highly interesting behavior that has evaded previous techniques. Several advantages of our current approach are illustrated, for example, in Figure 11. Immediately noticeable (as also in the other examples) is the extraordinary data density that resulted from automated experimentation and analysis, at a minimum manual effort of the operator. Yet, at

(18) Bloom, M.; Evans, E.; Mouritsen, O. G. *Q. Rev. Biophys.* **1991**, *24*, 293–397.

(19) Olbrich, K.; Rawicz, W.; Needham, D.; Evans, E. *Biophys. J.* **2000**, *79*, 321–327.

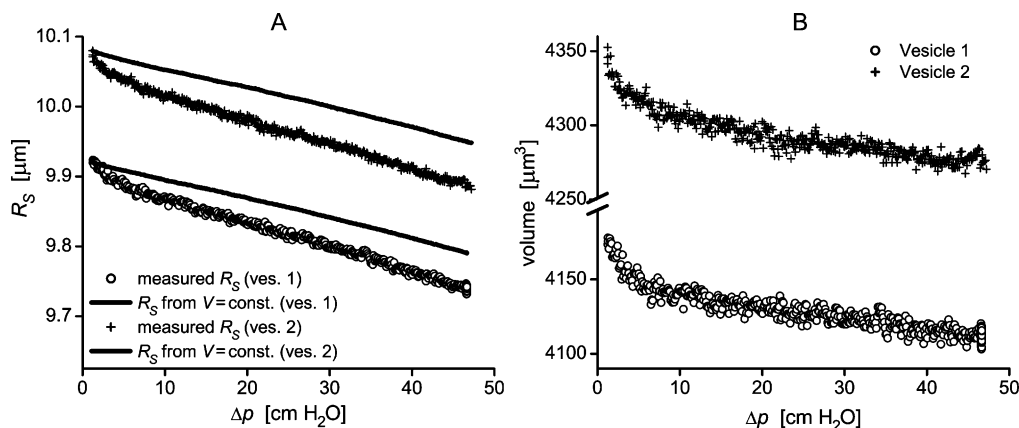


Figure 12. (A) Comparison of the directly measured R_S -values (symbols) to the values calculated using the constant-volume assumption (solid lines) for the same two aspiration experiments as in Figure 11. (B) Measured volume changes during these two aspiration experiments.

the used, moderate tension-loading rate of ~ 0.4 mN/m/s, the figure's individual data points were only recorded every ~ 0.6 s, approximately 1000 times slower than the instrument's full capacity! Furthermore, the smooth data curves generated by accurate, subpixel edge detection exhibit an unusually high signal-to-noise ratio for this type of pipet-aspiration data. This and the ability to remotely apply a large range of pressure rates (providing over 4 orders of magnitude in tension-loading rate) represent the main improvements over traditional techniques and have been instrumental in gaining new insight into membrane physics with the present approach. For example, in contrast to the general assumption that a lipid membrane can only stretch up to $\sim 2\%$ before it ruptures, the areas of the two membranes of Figure 11 were expanded by more than 5% at the moment of lysis. Applying 100 times faster tension ramps (~ 55 mN/m/s), we have occasionally observed unilamellar membranes that stretched as much as 13% before rupture! Clearly, the extent of possible membrane stretch, or conversely, the membrane's rupture tension, depends critically on the rate of tension loading. This kinetic entrapment phenomenon, which is central to dynamic tension spectroscopy,¹⁵ has become assessable only with the development of the present instrument.

Other advanced capabilities that are due to the availability of accurate, high-density, and low-noise experimental data include the direct extraction of the derivative of a measurable quantity (cf. Figure 10) and the identification of fast events with submillisecond resolution (Figure 9). In summary, preliminary measurements with the present instrument have revealed subtle and sometimes-unexpected aspects of membrane behavior that have led us to reexamine a number of physical properties of membranes, several of which are currently under investigation.

Acknowledgment. Long-time expert advice by Andrew Leung (University of British Columbia) is gratefully acknowledged. V.H. originally learned the basics of pipet aspiration in the laboratory of Richard E. Waugh (University of Rochester) and is thankful for a generous and skillful introduction to experimental membrane biophysics. The deep physical insight and creative ideas of Evan Evans (Boston University and University of British Columbia) have inspired many of the advances in technical development reported here. This work was supported by Canadian Institutes for Health Research Grant MOP-7477 and National Institutes of Health Grant HL65333, both to E. Evans.

LA047801Q